PROCEEDINGS, 42nd Workshop on Geothermal Reservoir Engineering
Stanford University, Stanford, California, February 13-15, 2017
SGP-TR-212

Overview and Preliminary Results from the PoroTomo project at Brady Hot Springs, Nevada: Poroelastic Tomography by Adjoint Inverse Modeling of Data from Seismology, Geodesy, and Hydrology

Kurt L. FEIGL

Department of Geoscience, University of Wisconsin-Madison, 1215 West Dayton Street, Madison, WI, 53706 United States

feigl@wisc.edu

The PoroTomo Team, including Michael A. CARDIFF(1), Xiangfang ZENG (1), Neal E. LORD (1), Chelsea LANCELLE (1), David D. LIM(1), Lesley PARKER(1), Elena C. REINISCH(1), S. Tabrez ALI(1), Dante FRATTA(1), Clifford H. THURBER(1), Herbert F. WANG(1), Michelle ROBERTSON(2), Thomas COLEMAN(3), Douglas E. MILLER(3), Janice LOPEMAN(4), Paul SPIELMAN(4), John AKERLEY(4), Corné KREEMER(5), Christina MORENCY(6), Eric MATZEL(6), Whitney TRAINOR-GUITTON(7), Samir JREIJ(7), Nicholas C. DAVATZES(8)

(1) University of Wisconsin-Madison, Department of Geoscience, Madison, WI, United States,
(2) Lawrence Berkeley National Laboratory, Berkeley, CA, United States,
(3) Silixa, Houston, TX, United States,
(4) Ormat Technologies Inc., Reno, NV, United States,
(5) University of Nevada Reno, NV, United States
(6) Lawrence Livermore National Laboratory, Livermore, CA, United States,
(7) Colorado School of Mines, Golden, CO, United States,
(8) Temple University, Philadelphia, PA, United States

http://geoscience.wisc.edu/feigl/porotomo/

Keywords: EGS, DAS, DTS, GPS, INSAR

ABSTRACT

In the geothermal field at Brady Hot Springs, Nevada, subsidence occurs over an elliptical area that is ~4 km by ~1.5 km. Highly permeable conduits along faults appear to channel fluids from shallow aquifers to the deep geothermal reservoir tapped by the production wells. Results from inverse modeling suggest that the deformation is a result of volumetric contraction in units with depth less than 600 m [*Ali et al.*, 2016].

Characterizing such structures in terms of their rock mechanical properties is essential to successful operations of Enhanced Geothermal Systems (EGS). The goal of the PoroTomo project is to assess an integrated technology for characterizing and monitoring changes in the rock mechanical properties of an EGS reservoir in three dimensions with a spatial resolution better than 50 meters. The targeted rock mechanical properties include: saturation, porosity, Young's modulus, Poisson's ratio, and density, all of which are critically important characteristics of a viable EGS reservoir.

In March 2016, we deployed the integrated technology in a 1500-by-500-by-400-meter volume at Brady Hot Springs. The 15-day deployment included four distinct time intervals with intentional manipulations of the pumping rates in injection and production wells. The data set includes: active seismic sources, fiber-optic cables for Distributed Acoustic Sensing (DAS) and Distributed Temperature Sensing (DTS) arranged vertically in a borehole to ~400 m depth and horizontally in a trench 8700 m in length and 0.5 m in depth; 244 seismometers on the surface, three pressure sensors in observation wells, continuous geodetic measurements at three GPS stations, and seven images for interferometric synthetic aperture radar (InSAR). To account for the mechanical behavior of both the rock and the fluids, we are developing numerical models for the 3-dimensional distribution of the material properties.

The work presented herein was funded in part by the Office of Energy Efficiency and Renewable Energy (EERE), U.S. Department of Energy, under Award Number DE-EE0006760.

1. INTRODUCTION

In the geothermal field at Brady Hot Springs, Nevada, subsidence occurs at a rate of the order of a centimeter per year over an elliptical area that is ~4 km by ~1.5 km, as measured by satellite interferometric synthetic aperture radar (InSAR) and mapped in Figure 1. Results from inverse modeling suggest that the deformation is a result of volumetric contraction in units with depth less than 600 m. [*Ali et al.*, 2016]. Highly permeable conduits along faults appear to channel fluids from shallow aquifers to the deep geothermal reservoir tapped by the production wells, as sketched in Figure 2.

The objective of the PoroTomo project is to assess an integrated technology for characterizing and monitoring changes in an enhanced geothermal system (EGS) reservoir in three dimensions with a spatial resolution better than 50 meters. The targeted characteristics

include: saturation, porosity, Young's modulus, Poisson's ratio, and density, all of which are "critically important" to a viable EGS reservoir (DOE GTO, 2014). Estimating these parameters and their uncertainties will contribute to the overarching goal of characterizing the reservoir in terms of its effective permeability and/or fracture transmissivity.

The technology performance metric for the project is resolution in meters of a feature in the modeled 3-D distribution of a rock mechanical property (e.g., Poisson's ratio), as determined by the dimension of a visible checkerboard pattern at 200 m depth in a test using simulated data. Resolution is controlled by: the number of parameters to be estimated in the inverse problem, the number of measurements, and the distribution of the sensors. For seismic data, the wavelength and distribution of the sources also play crucial roles.

During Phase I of the project, we accomplished a proof of concept. We have validated the computational analysis techniques by adapting and applying them to existing data sets [*Ali et al.*, 2016; *Lancelle*, 2016; *Lord et al.*, 2016a; *Zeng et al.*, 2017a].

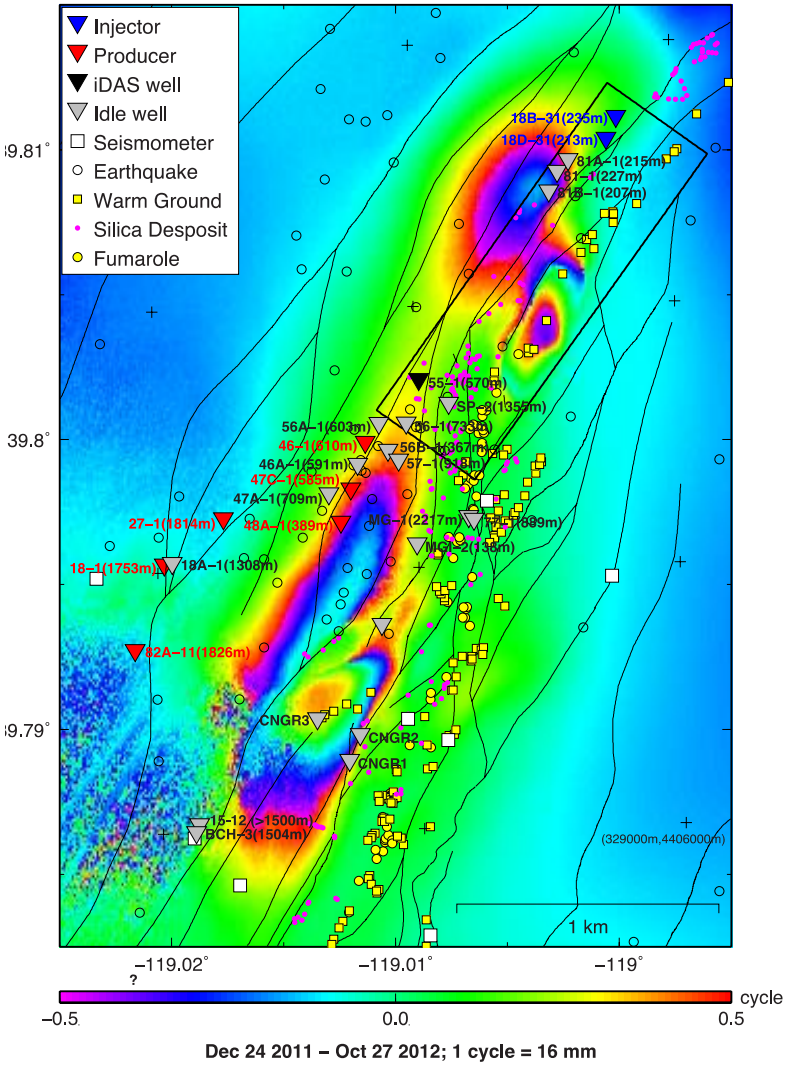

Figure 1. Map showing location of the Brady Hot Springs geothermal field, with faults (thin black lines, [*Faulds et al.*, 2010], surface hydrothermal activity, including fumaroles (yellow circles), warm ground (yellow squares), and silica deposits (magenta circles) from precise field mapping [*Coolbaugh et al.*, 2004]. Injection wells are shown by blue triangles and producing wells are shown by red triangles. Fiducial crosses indicate 1000-meter grid in easting and northing of the Universal Transverse Mercator (UTM) projection (Zone 11). The SAR interferogram in the background shows the change in wrapped phase over the 308-day interval from December 24, 2011 to October 27, 2012. One colored fringe corresponds to one cycle of phase change, or 16 mm of range change. The dotted and dashed grey line delimits the broad subsiding zone. The black rectangle delimits the study area of the PoroTomo project.

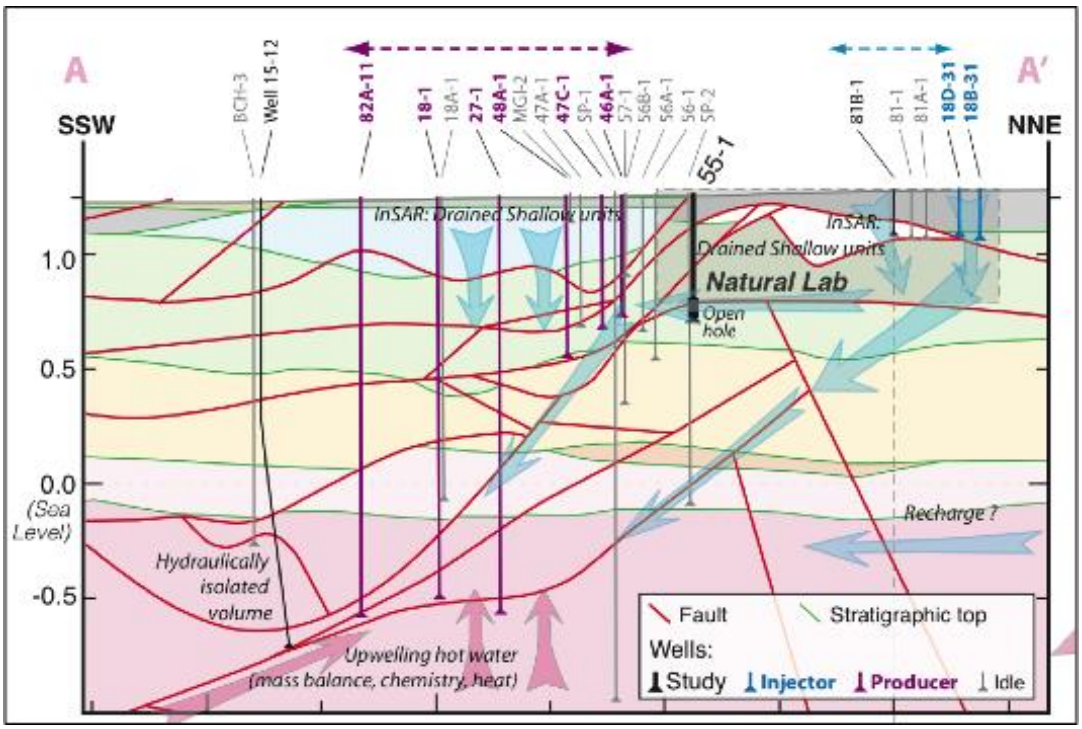

Figure 2. Sketch of vertical cross section, showing the key idea that highly permeable conduits along faults channel fluids from shallow aquifers to the deep geothermal reservoir tapped by the production wells. Vertical cross section based on geologic model of Jolie, Moeck and Faulds and geologic mapping by Faulds [*Faulds et al.*, 2004; *Faulds et al.*, 2006; *Faulds*, 2011; *Shevenell et al.*, 2012; *Jolie et al.*, 2015]. Elevation in km. V:H = 1:1.

2. DEPLOYMENT AT BRADY HOT SPRINGS DURING MARCH 2016

In Phase II of the project, we are working to demonstrate a prototype of an integrated technology at the EGS field at Brady Hot Springs, Nevada. The study area is a shallow volume with length ~1500 m, width ~500 m, and depth ~400 m, as delimited by the black rectangle in Figure 1. In March 2016, we deployed the proposed technology during four distinct time intervals, as illustrated in Figure 3. Between each measurement interval, the hydrological conditions were intentionally manipulated by modifying the rates of pumping in the injection and production wells. By comparing the four sets of results, we expect to quantify any temporal changes in the characteristics of the study volume.

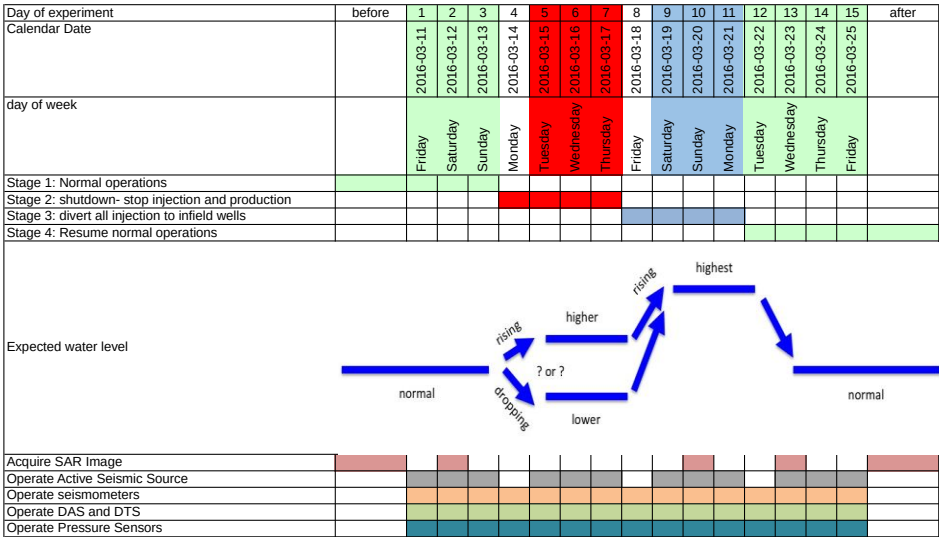

Figure 3. Schedule of operations during deployment at Brady Hot Springs in March 2016, showing pumping operations (upper rows), expected level of groundwater (arrows), and data streams (lower rows).

We are analyzing measurements from three data sets: (1) seismic waveforms recorded by seismometers and distributed acoustic sensors (DAS); (2) the deformation of the Earth's surface recorded by satellite geodesy, including the Global Positioning System (GPS) and Interferometric Synthetic Aperture Radar (InSAR); and (3) time series of hydraulic pressure, flow, and temperature measured in wells for production, injection, or observation. Metadata describing each of these data sets are available at the Geothermal Data Repository (GDR): https://gdr.openei.org/search?q=porotomo&submit=Search. Subsets of the data are currently publically available at the GDR, as listed in Figure 4. All of the data will become available to the public on October 1st, 2017, when the DOE award concludes.

Data Stream	Notes	URL
Geology	Earthvision database by Siler et al.	https://gdr.openei.org/
Production	Pressure and Volume	https://gdr.openei.org/
Pressure and Temperature	In 3 observing wells	https://gdr.openei.org/
INSAR (56 mm wavelength)	ESA's Sentinel 1-A & 1-B	https://scihub.copernicus.eu/
INSAR (32 mm wavelength)	DLR's TerraSAR-X and TanDEM-X	https://winsar.unavco.org/
GPS	1 estimate/day; 3 cont. stations	https://gdr.openei.org/
Vibroseis	SEG-Y files for pilot and pad	https://gdr.openei.org/
Nodal Seismometers	hourly SAC files; 238 stations	https://gdr.openei.org/
DAS - horizontal in trench	8700 meters, SEG-Y format	ftp://roftp.ssec.wisc.edu/porotomo/
DAS - vertical in borehole	400 meters, SEG-Y format	ftp://roftp.ssec.wisc.edu/porotomo/
DTS - vertical in borehole	400 m L0 in XML, L1 in CSV	ftp://roftp.ssec.wisc.edu/porotomo/
value added by partnerships:		
DTS - horizontal in trench	9000 m, L0 in XML, L1 in CSV	ftp://roftp.ssec.wisc.edu/porotomo/
permaseis	Permanent LBL seismic network at Bra	http://www.ncedc.org/
UAV	Optical photogrammetry	http://ctemps.org/

Figure 4. List of PoroTomo data sets.

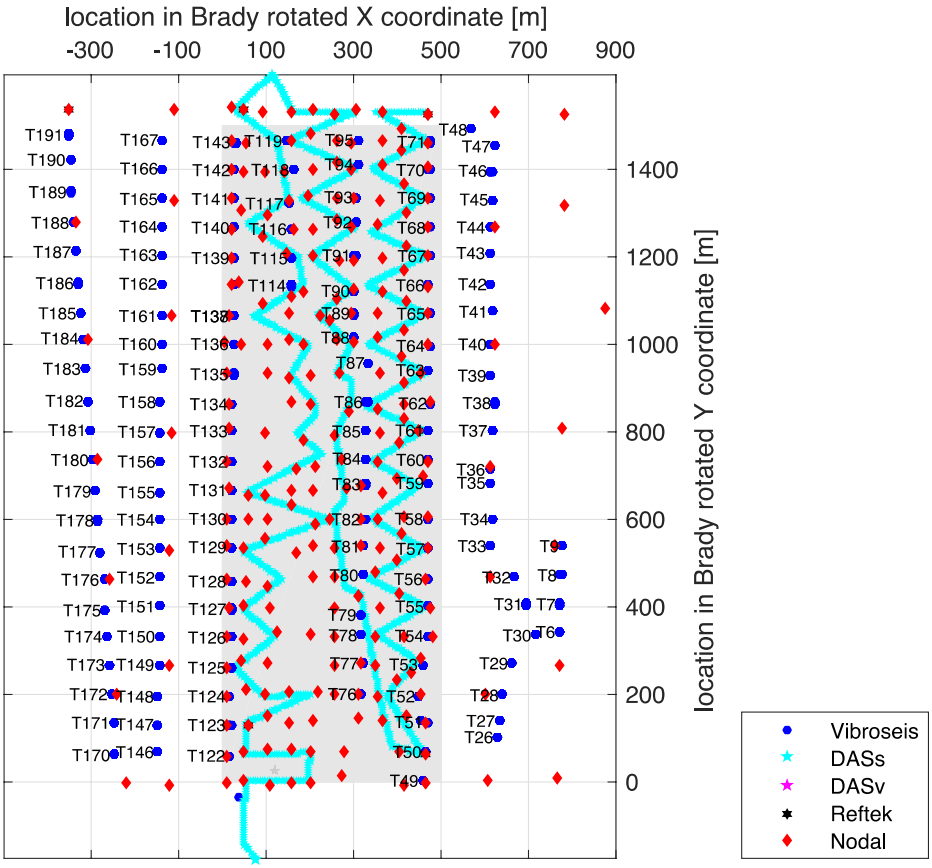

Figure 5. Map of study area, showing volume targeted for tomography (gray shading), vibroseis points (blue hexagons, labeled T*nnn*), Nodal seismometers (red diamonds), and fiber-optic cable (cyan line) for distributed acoustic sensing (DAS) and distributed temperature sensing (DTS). A separate fiber optical cable for DAS and DTS was deployed vertically in the borehole of Well 56-1 (star located near [X,Y] = [100, 0] m). The Y-axis of the rotated coordinate system is approximately parallel to the northeast-striking fault system.

In the following sections, we describe the networks of instrumentation deployed in March 2016. The 3-dimensional position of each instrument was surveyed with centimeter-level accuracy using Real Time Kinematic (RTK) GPS. In addition, we present some preliminary results from each data set.

Hydrology

We monitored pressure and temperature at several wells. The details of the instrumentation as well as the metadata describing the monitoring boreholes are available on the GDR [Lim, 2016]. Briefly, the monitoring locations consisted of a shallow well near where water is re-injected (81B-1), a deep well near the main area of production (56A-1), and a well located halfway between these two points (SP-2). In addition, pumping data, including flow rates, temperature and pressure are available for the production and injection wells that were in operation during the deployment are also available on the GDR [Akerley, 2016].

The time series of pressure recorded in three monitoring wells are shown in Figure 6. Of these three wells, only Well 81B-1 has a water level that coincides with a screened interval, meaning that this well is likely most representative of the local depth to water. The pressure recorded in Well 81B-1, for purposes of initial analysis, was converted to an equivalent water level (in meters above WGS84 ellipsoid) using standard values for density; this approach was then verified against other site data including pre-test pressure/temperature (P/T) logs, which indicate a strong change in the pressure gradient at the estimated water table depth. During site shutdown (Stage 2), we estimate that the elevation of the water level near these injection wells dropped by roughly ~5 m. The water level then rose again by as much as ~20 m when all of the produced brine was re-injected within the study area (Stage 3). Finally, the water level dropped by ~10 m after the injection returned to normal operations in Stage 4, sending approximately a third of the water to an injection well located more than 3 km away from the study area. We note that estimating the absolute elevations of water levels in the reservoir is complicated by issues such as the difference in gas pressure between a capped well and the surrounding formation (which may or may not be in communication with the atmosphere). Thus, while absolute elevations of water levels are likely subject to an error of several meters, the relative changes in pressure are robust and easily detected.

The pressure fluctuations recorded in well 56A-1 are of the same order of magnitude, but with opposite sign, as those in Well 81B-1. These measurements indicate that the pressure change disturbance is comparable in this region, though opposite in sign since well 56A-1 is in close proximity to the pumping wells rather than the injection wells. Whether water *pressure* measurements in 56A-1 are representative of reservoir water *level* changes is not clear, due to the fact that 56A-1 is screened at significant depth. To interpret the pressure values recorded in Well 56A-1 in terms of the reservoir water level, one may assume that the reservoir is vertically equilibrated as a first approximation.

Our next step in analyzing the hydrological data sets will be to estimate reservoir properties from the time series of data, and assess whether impacts of heterogeneity are apparent. In this analysis, we will also compare traditional transient numerical modeling approaches against a phase-domain modeling approach that tracks pressure responses in terms of amplitude and phase lag, as performed previously at a site in Idaho [e.g., *Cardiff et al.*, 2013; *Lim et al.*, 2015].

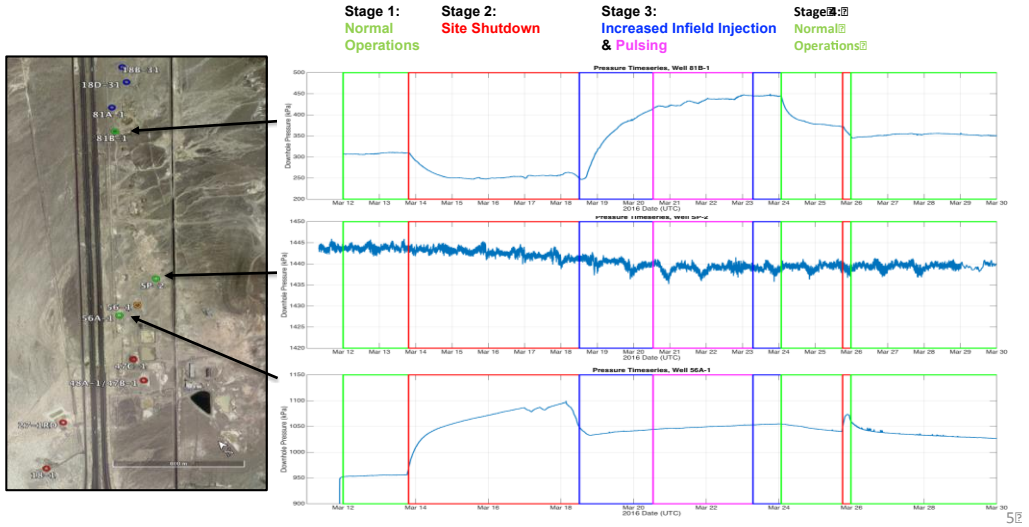

Figure 6. Time series of pressure records showing the response to four stages of pumping operations at recorded in three monitoring boreholes: Well 81B-1, near the injection wells at the northeast end of the study area (upper panel); Well SP-2, on the southwest side of the fault system in the center of the study area (middle panel), and Well 56A-1 near the production wells at the southwest end of the study area (lower panel). For interpretation, a change of 100 kPa of pressure corresponds to change in water level of the order of 10 m.

Geodesy – GPS

Three GPS stations operated continuously during the deployment. Station BRD1 was installed on the head of completed Well 18-1 on March 10th 2016. It is located inside the study area, near the center of the area undergoing rapid subsidence, as mapped by InSAR. GPS stations BRAD and BRDY are located outside the study area at distances of approximately 5 and 3 km from BRD1, respectively. All three GPS stations are part of the MAGNET network operated by the Geodesy Lab at the University of Nevada in Reno. The procedures for analyzing the data have been described previously [*Blewitt et al.*, 2013]. An example of the time series of the relative position of station BRD1 with respect to BRDY appears in Figure 7. Figure 8 shows the rate of relative displacement, i.e., the vertical velocity of BRD1 with respect to BRDY. It suggests that the shutdown of pumping in Stage 2 and/or the diversion of all produced water back into the injection wells within the study area during Stage 3 produced a vertical displacement of several millimeters. Next, we evaluate the significance of the two transitions: (a) between Stage 1 and Stages 2&3 on March 14th (b) Stages 2&3 vs. Stage 4 on March 24. For each transition, the null hypothesis (that the rate does not change) fails to be rejected by a T-test with 95 percent confidence.

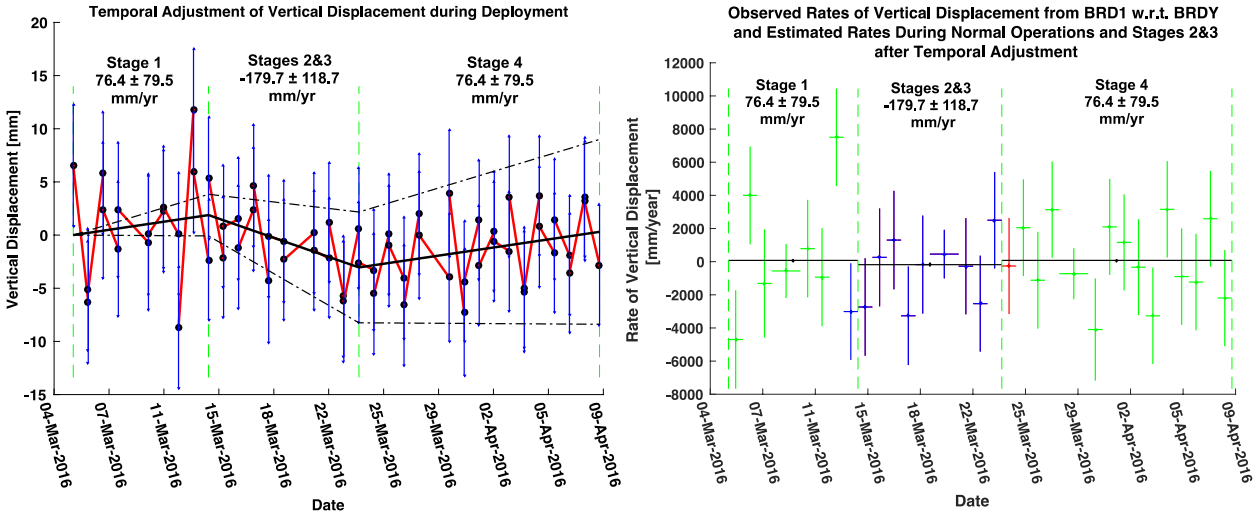

Figure 7. At left: time series of vertical component of relative position of GPS station BRD1 with respect to station BRDY. The black line shows a model estimated by the temporal adjustment procedure [*Reinisch et al.*, 2016b]. The model is parameterized as piecewise-linear polynomial with breaks at the start of Stage 2 and end of Stage 3. We constrain the rates of Stages 1 and 4 to be equal, in accordance with the corresponding temporal adjustment of volume change derived from InSAR measurements (Figure 9). Pair-wise measurements are indicated in red, with 1-sigma uncertainties denoted in blue. Modeled displacement is shown by the solid black line, with upper and lower uncertainties denoted with dashed black lines. The start and end of the dataset as well as the start of Stage 2 and end of Stage 3 are denoted with green dashed lines [*Reinisch et al.*, 2016a].

Figure 8. At right: Rates of vertical displacement of GPS station BRD1 with respect to BRDY. Rates estimated by temporal adjustment [*Reinisch et al.*, 2016b] during normal operations (Stage 1 and Stage 4) and during Stage 2&3 are shown with black lines. Observed rates corresponding to pairs with a starting epoch during stages 2&3 are colored in red. Rates corresponding to pairs with an ending epoch during stages 2&3 are colored in blue. All other pairs are colored in green. Uncertainties are denoted with vertical error bars. The start and end of the dataset as well as the start of Stage 2 and end of Stage 3 are denoted with green dashed lines.

Geodesy – InSAR

Interferometric analysis of synthetic aperture radar images (InSAR) is a geodetic technique that calculates the interference pattern caused by the difference in phase between two images acquired by a satellite radar sensor at two distinct times. The resulting interferogram is a contour map of the change in distance between the ground and the radar instrument. These maps provide a spatial sampling density of ~100 pixels/km^2, a precision of ~10 mm, a registration accuracy of ~10 m, and an observation cadence of ~1 pass/week. This remote-sensing tool has been demonstrated and validated for many actively deforming areas, including Brady [e.g., *Massonnet and Feigl*, 1998; *Oppliger et al.*, 2004; *Ali et al.*, 2016].

Two satellite missions acquired SAR images covering the study area at Brady during the deployment in March 2016. The X-band SAR sensor aboard the TerraSAR-X [*Pitz and Miller*, 2010] mission operated by the German Space Agency (DLR) acquired images on March 1, 4, 12, 20, 23, and 26, 2016. These images extend the InSAR time series analyzed previously [*Ali et al.*, 2016]. The C-band ASAR sensor aboard the Sentinel-1A satellite mission [*Salvi et al.*, 2012; *Torres et al.*, 2012], operated by the European Space Agency (ESA), acquired SAR data on March 2, 9, 26 2016 in IW mode under a protocol named Terrain Observation with Progressive Scans (TOPS).

Applying the analysis procedure described by Ali et al. [2016], we find that the two changes in the rate of volumetric decrease (at the start of Stage 2 and the end of Stage 3) are significantly different from zero with 95% confidence, as shown in Figure 9.

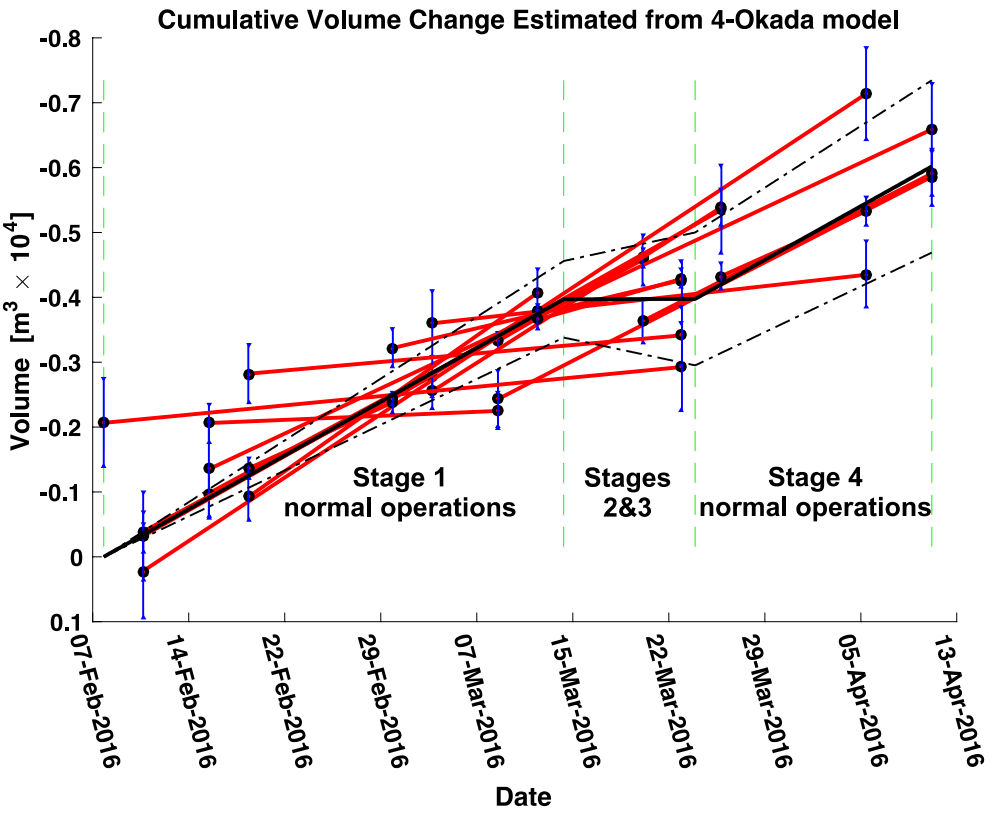

Figure 9. Change in volume of rock, as calculated by temporal adjustment of estimates of an elastic model including four shrinking, rectangular dislocations [*Reinisch et al.*, 2016a].

Seismology

A crew from the University of Texas-Austin operated a vibrating source named T-REX. The vibration protocol included three sweeps for each of P, transverse S, and longitudinal S at each of approximately 200 locations during each of the four stages of the 15-day field experiment. Using associated coder/decoder telemetry units, the vibroseis truck operated in synchronization with the DAS array and the conventional seismometers. For each of the three modes, the vibroseis source made three sweeps over 20 seconds. Each sweep increased in frequency from 5 Hz to 80 Hz

The seismic instrumentation included 238 Zland 3-component sensors manufactured by FairfieldNodal. Each of these instruments (dubbed "Nodals") has a corner frequency of 5 Hz, a 24-bit digitizer with a dynamic range of 127 dB, and a timing accuracy of ±10 microseconds from a GPS receiver [*FairfieldNodal*, 2015]. Between March 11 and March 26, 2016, these instruments operated and recorded autonomously and continuously with sampling interval of 0.002 s (i.e. a sampling frequency of 500 samples per second) for the entire two-week deployment without any human intervention. Arrays of *single-component*, 10-Hz Nodal instruments have been utilized for many scientific projects, including at Long Beach, CA [*Lin et al.*, 2013], but the PoroTomo experiment is one of the first academic uses of the newer *three-component* 5-Hz Nodal instruments. Figure 10 shows an example of the correlation between the vibroseis source and the seismograms recorded by the Nodal seismometers.

The seismic network also included six 3-component seismic stations from the consortium named Portable Array Seismic Studies of the Continental Lithosphere (PASSCAL). Each station included a L28 model, 4.5-Hertz, 3-component geophone, Reftek RT130 seismograph, and a GPS timing clock.

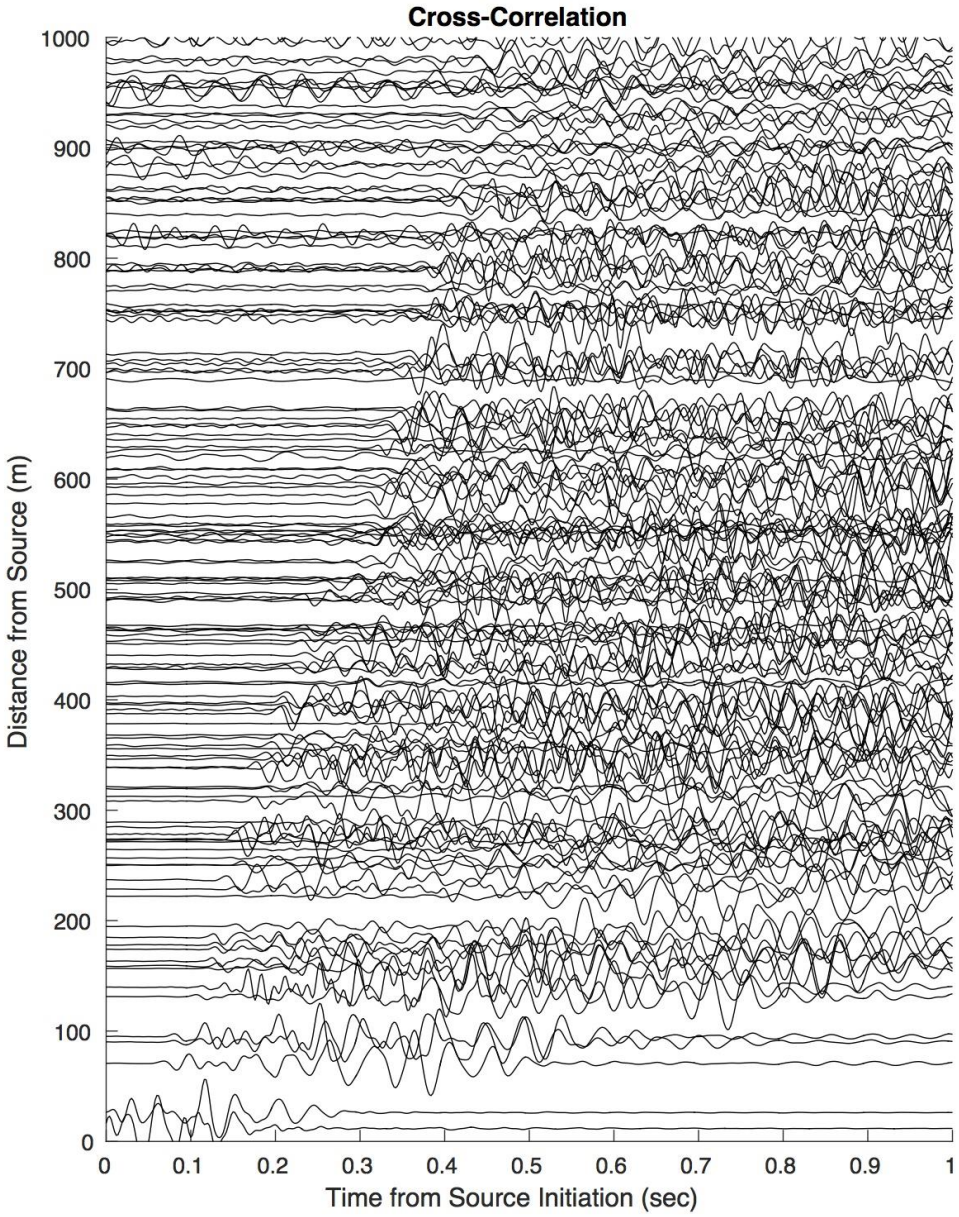

Figure 10. Cross-correlation of the vertical components of seismograms against signal recorded at the vibe truck. Cross-correlation results show discernable P-wave arrivals up to 1000 m from the source location. This corresponds to 74.5% of the source-to-station pairs. This example record section shows sweeps 0680, 0681, and 0682 (stacked) at vibe point 144 [*Parker et al.*, 2016].

Seismology: Horizontal-to-Vertical Spectral Ratio for Estimating Thickness of Sedimentary Deposits

By calculating the ratio of the spectral power for the horizontal component of the seismograms with respect to that of the vertical component, we can estimate the thickness of the uppermost (unconsolidated) layer and thus the depth to (stiff) bedrock [*Nakamura*, 1989; *Haefner et al.*, 2010]. The thickness Z of the uppermost layer is related to the frequency of peak (f_r) on the HVSR spectra by $Z = Vs/(4f_r)$ where Vs is the shear wave velocity of the sediment layer.

Using Vs estimates from Zeng et al. (2017), we estimate that the depth to bedrock varies between 8 and 105 meters, as shown in Figure 11. The uppermost deposits are very heterogenous and include diatomaceous earth, silt, sand, and hardened silica associated with the presence of fumaroles, as observed by field mapping [*Faulds and Garside*, 2003; *Coolbaugh et al.*, 2004; *Faulds et al.*, 2004; *Faulds et al.*, 2010]. These heterogeneities restrict the applicability of the technique because it assumes horizontally layered media.

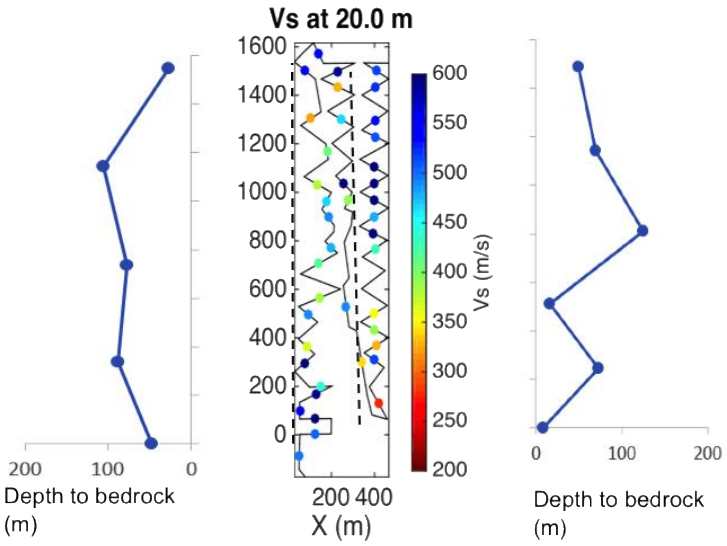

Figure 11. Estimated depth to stiff bedrock along the dashed black lines found using from the horizontal-to-vertical spectral ratio. The assumed shear wave velocity Vs (middle panel) was found by Zeng et al. (2017b) using ambient noise correlation functions at a depth of 20 m.

Seismology: ambient noise tomography on a dense array of nodal seismometers

Figure 12 shows results from performing ambient noise tomography on the Nodal seismograms [*Zeng et al.*, 2016; *Zeng et al.*, 2017b]. The ambient noise cross-correlation functions clearly show surface waves. The resolution is good at the scale of ~100 m. The average group velocity at 4 Hz indicates strong spatial heterogeneities at depths of the order of 100 meters below the surface. The areas of anomalously slow velocity appear to coincide approximately with the areas of subsidence measured by InSAR, as discussed in more detail by Zeng et al. [2017b].

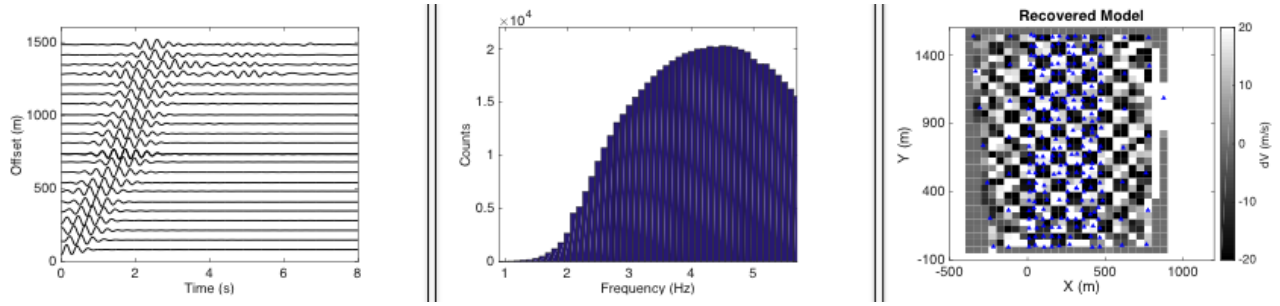

Figure 12. Results from ambient noise tomography using the Nodal seismograms [*Zeng et al.*, 2016; *Zeng et al.*, 2017b]. The ambient noise cross-correlation functions (left) show a clear signal from a surface wave. Using the frequency-time analysis (FTAN) method, approximately 15 thousand estimates of group velocity were obtained (middle). The 2-by-2 checkerboard was successfully recovered in most of the study area (right).

Distributed Acoustic Sensing (DAS)

We deployed an "intelligent" Distributed Acoustic Sensing (iDAS^{TM}) system, which uses a continuous length of fiber-optic cable as an array of seismic sensors [e.g., *Parker et al.*, 2014]. This technology transmits pulses of light into the fiber and records the response from its Rayleigh backscatter. The resulting measurement is sensitive to the rate of transient strain along the axis of the cable.

At Brady, we deployed the first DAS array in a geothermal field in North America, including 8700 meters of DAS cable buried horizontally in a shallow trench and 400 meters of DAS cable hanging vertically in Well 56-1. The data were recorded continuously, archived in 30-second files in SEG-Y format [*Barry et al.*, 1975], and submitted to the Geothermal Data Repository (https://gdr.openei.org/). More than 60 Terabytes of DAS data were collected over the four stages of the PoroTomo experiment in March 2016.

To understand the DAS recordings, we review a few of their characteristics [*Bakku*, 2015; *Daley et al.*, 2015]. DAS measures the strain rate $\dot{\varepsilon}$ in the fiber by averaging its elongation over a segment of cable (called the "gauge length") during a temporal sampling interval. The elongation represents the phase shift of the backscattered light pulse. These data were written with dimensions of radians per

millisecond in the SEG-Y files. In this DAS system, one radian of phase change corresponds to 116 nanometers of elongation. The wavelength of the laser light is 1550 nanometer. The temporal sampling interval was set to 1 millisecond and the spatial sampling length was set to 1 meter. The spatial resolution of the DAS strain rate measurement equals the gauge length of 10 m.

In terms of seismology, we consider the motion of a particle oscillating in a plane wave with displacement $u = U\exp\left[-i\left(\omega t - kz\right)\right]$, where t is time, ω is angular frequency, k is spatial wavenumber and U is amplitude. The strain ε and particle velocity $\dot{u}$ are related by:

$$\varepsilon = \dot{u} / c \tag{1}$$

where $c = k/\omega$ is the phase velocity of the plane wave [*Benioff and Gutenberg*, 1952; *Daley et al.*, 2015]. Using equation (1), we can compare the time series recorded by DAS with those recorded by a conventional seismometer. To find the transient strain ε in the fiber, one can integrate the DAS strain rate $\dot{\varepsilon}$ in the fiber with respect to time. For the raw DAS data recorded at Brady in the SEG-Y files submitted to the GDR, this operation involves forming the cumulative sum of the strain rate (in radians per 10-meter gauge length per 1-milliscond time sample) and multiplying by a factor of 11.6 nanostrain per radian. The result is the strain in nanostrain or parts per billion.

An example appears in the left panel of Figure 13**.** It shows the transient strain recorded by DAS channel 544 about 25 seconds after a magnitude 4.3 earthquake that occurred near Hawthorne, Nevada on March 21, 2016 at 7:37 UTC.

On the other hand, a conventional seismometer couples most directly to the velocity $\dot{u} = du/dt$ of a particle in the ground, where u is its displacement. To obtain the particle velocity along the axis of the fiber optic cable from the seismograms recorded at Nodal station 151 at Brady, we combine their two horizontal components. The resulting particle velocity appears in the right panel of Figure 13 that also shows the time interval following the Hawthorne earthquake. Both the DAS trace and the Nodal seismogram clearly show the P-wave and the S-wave.

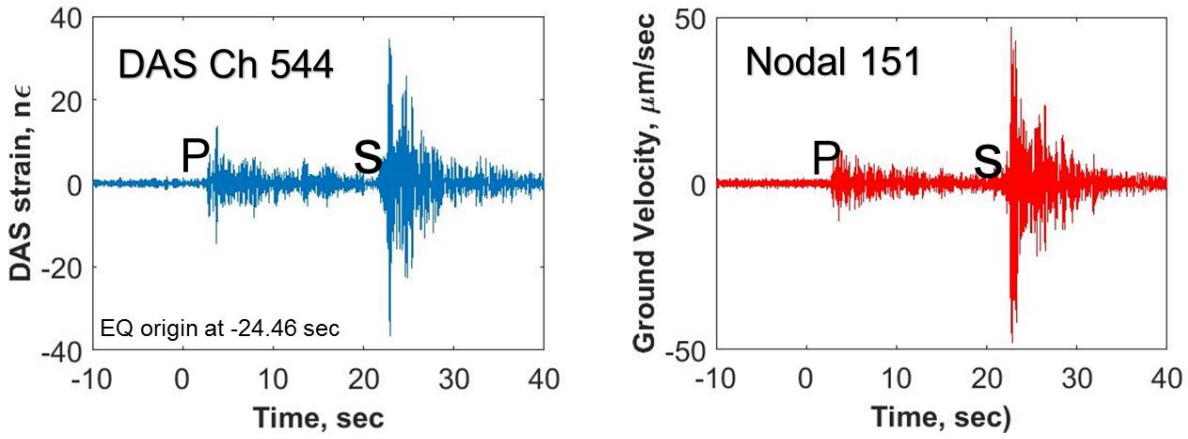

Figure 13. Time series of ground motion at Brady following the magnitude 4.3 earthquake that occurred near Hawthorne, Nevada, as recorded by DAS channel 544 (left panel) and a co-located Nodal seismometer at station N151 (right panel). The time scale is such that t = –24.46 seconds is the earthquake origin time of 7:37 UTC on March 21, 2016.

To find the particle velocity $\dot{u}$, we analyzed DAS data from 128 channels within a 148-meter-long segment of fiber-optic cable by forming a 2-dimensional Fourier transform and rescaling by the phase velocity $c = k/\omega$ at each temporal frequency ω and spatial wavenumber k. (A regularization term was included in the denominator.) Then, the inverse Fourier transform gave the component of fiber particle velocity shown by the blue trace in Figure 14. This trace estimates the component of particle velocity aligned with the cable.

After alignment with the cable axis (as described above and shown in the right panel of Figure 13), the data from Nodal seismometer 151 were processed to compensate for its response function, which is dispersive at frequencies less than its resonant frequency of approximately 5 Hz. Figure 14 compares the resulting time series of ground particle velocity estimated from the two sensors. Further comparisons of the ground motions recorded by the two arrays (DAS cable and Nodal seismometers) are underway [*Wang et al.*, 2016].

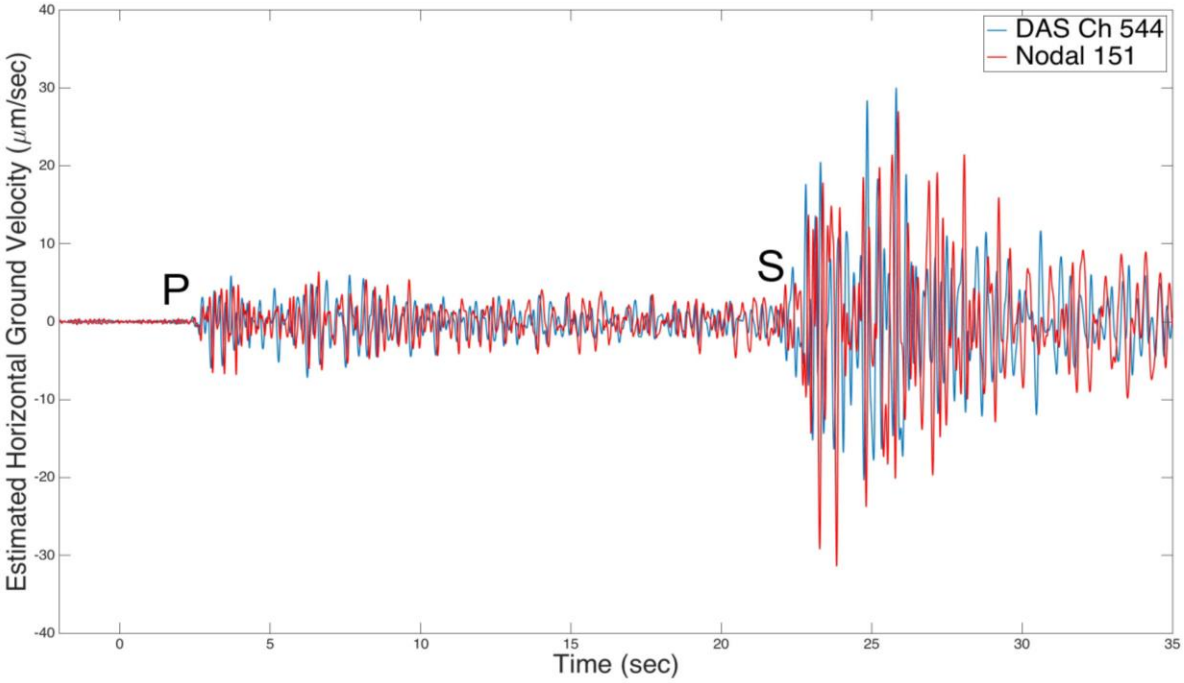

Figure 14. Time series of particle velocity along the cable at Brady as recorded by DAS channel 544 (blue) and a co-located Nodal seismometer at station N151 (red). The time scale is such that *t* = –24.46 seconds is the origin time of 7:37 UTC on March 21, 2016 for the magnitude 4.3 earthquake that occurred near Hawthorne, Nevada.

Seismology: Estimating (dispersive) surface wave (phase) velocity from vibroseis sources to DAS recordings

The dispersion curve in Figure 15 shows the surface wave phase velocity as a function of half-wavelength for vibroseis sweeps at two locations, T137 and T72, and then recorded by DAS. The estimation procedure is multichannel analysis of surface waves (MASW) [*Lord et al.*, 2016b]. The shear-wave phase velocity varies from 500 to 250 m/s. These waves penetrate to 40 m depth. The shear-wave velocity increases with wavelength at both locations. The shear-wave velocities are lower at station T137 than T72. Station T137 is located at a lower elevation than station T72 with a greater thickness of poorly consolidated alluvial deposits.

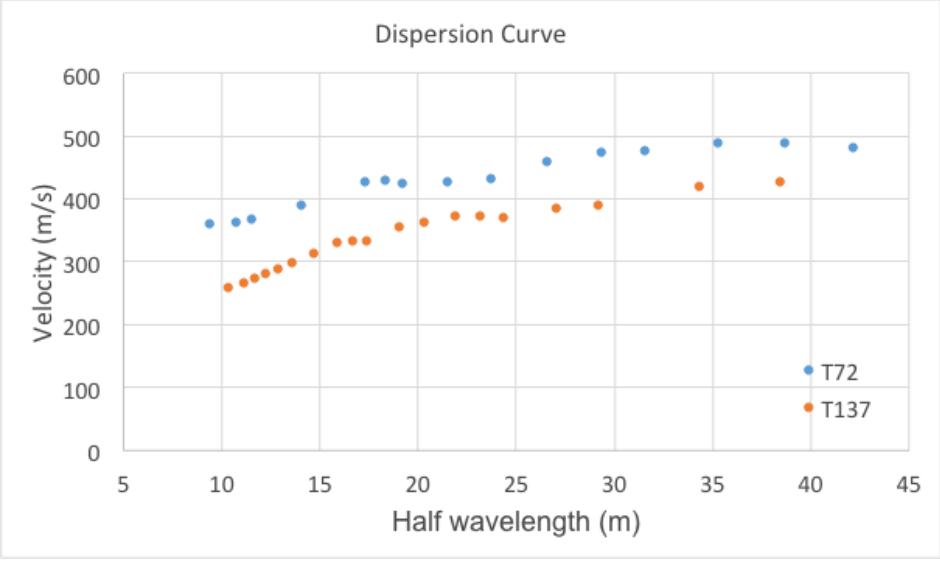

Figure 15. Dispersion curve, showing shear-wave phase velocity as a function of half wavelength from multichannel analysis of surface waves (MASW) recorded by DAS [Lord et al., 2016b].

Seismology: DAS data recorded in a borehole

Figure 16 shows signal as a function of depth and time from sweeps at two different vibroseis stations recorded by DAS in a vertical borehole in Well 56-1. The raw data were converted to fiber strain and correlated with the motion of the vibrating baseplate recorded by an accelerometer aboard the vibroseis truck. The two panels compare responses from two stations with similar offsets (about 260 m) from the well. The red arrows indicate the direct compressional arrival in each panel. The blue arrows indicate a down-going shear signal. The compressional signals match more closely than the shear in this case. This is likely due to differences in the near-surface properties in the vicinity of the two source locations. An up-going shear signal converted from a down-going P wave at a boundary near 300-m depth is evident in both panels, although more clearly evident in the left-hand panel.

The zone between depths 0 and 150 m is dominated by reverberation at 4 km/sec. This reverberation is likely to be due to an un-cemented portion of the well casing. Alternatively, the reverberation may also be due to a section of DAS cable that is hanging freely inside the wellbore with little or no coupling to the casing.

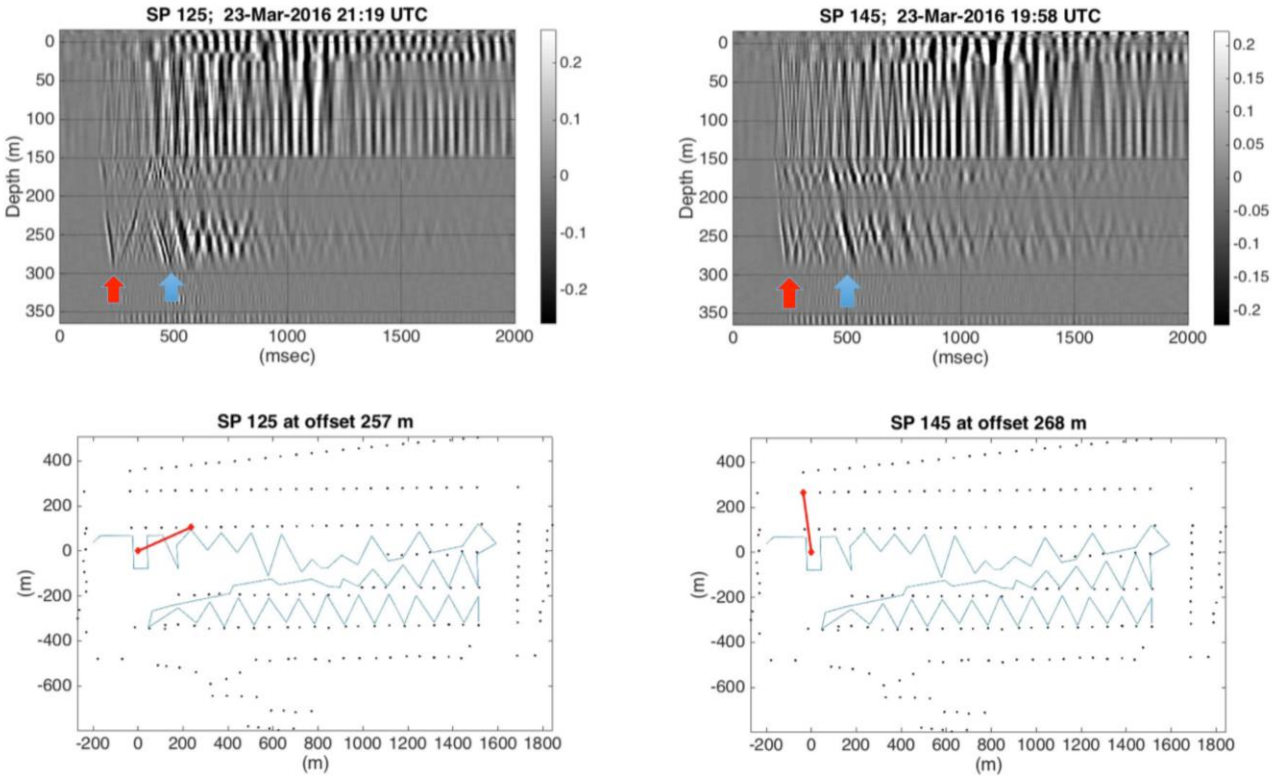

Figure 16. Examples of signal as a function of depth and time from sweeps at two different vibroseis stations recorded by DAS in a vertical borehole in Well 56-1. The raw data were converted to fiber strain and correlated with the motion of the vibrating baseplate recorded by an accelerometer aboard the vibroseis truck.

Distributed Temperature Sensing

The same fiber optic cables also performed distributed temperature sensing – DTS [e.g., *Coleman*, 2013]. An example of a vertical temperature profile from Well 56-1 appears in Figure 17. The temperature of the water and sand in the well increased rapidly following injection of cold water into the well at the time the fiber optic cable was installed. The highest temperatures form a 50-m thick zone around a depth of 250 meters. Enlarging the final ten hours of the data record, we see the temperature fluctuating after pumping operations resumed late on March 25th, 2016. Similar fluctuations in pressure occurred in nearby well 56-A1, as shown in Figure 6.

This observation is consistent with the hypothesis that the two wells have similar water levels and were similarly affected by the resumption of pumping operations.

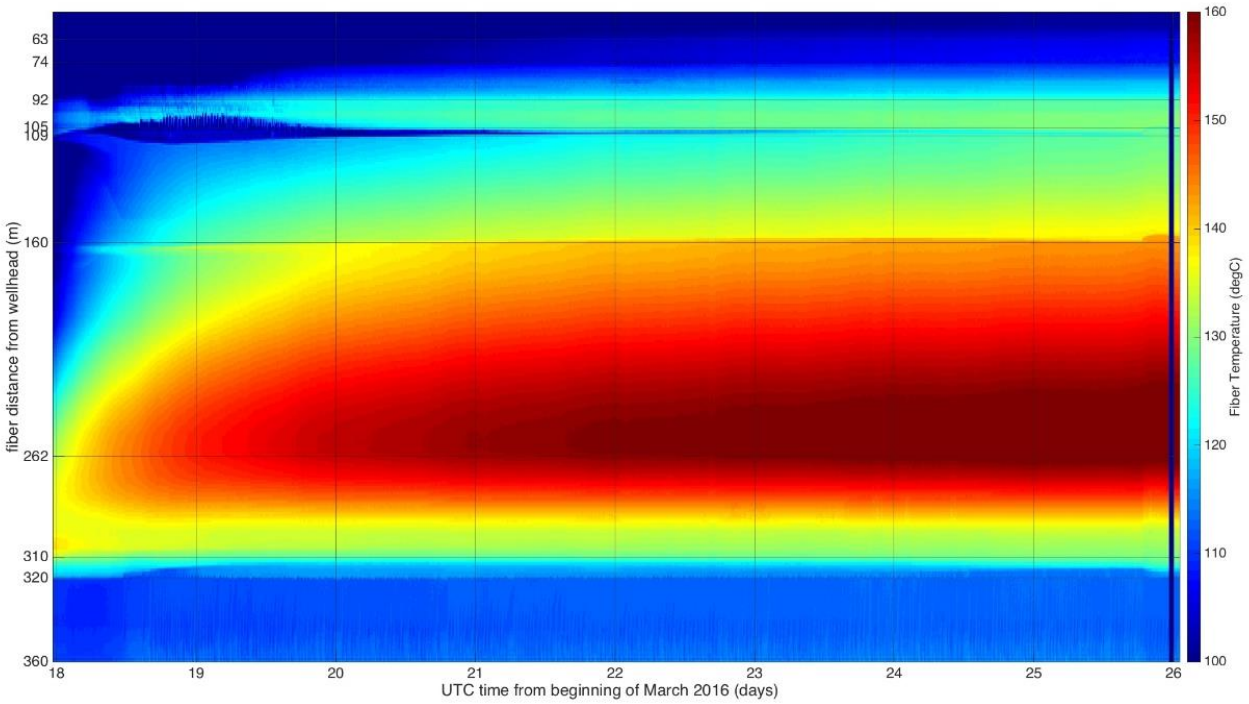

Figure 17. Temperature as a function of time measured by DTS in Well 56-1 between March 18 and 26, 2016 following injection of cold water into the well during the installation on March 17th.

CONCLUSIONS

After completing the data analysis, we plan to perform inverse modeling with a Bayesian, adjoint-based approach. The comparison will also assess the statistical uncertainty and resolution of the results. The expected outcome of Phase II is a validated small-scale prototype that will provide the technical specifications required to deploy the technology in a deeper, full-scale EGS field. The technical specifications of the integrated technology include the: 3-dimensional location, temporal sampling rate, observing time interval, spatial density, and measurement precision of each of the sensor networks (e.g., seismometers, DAS, distributed temperature sensors, pressure gauges, InSAR), as well as the configuration of the active seismic sources. The technical specifications could be scaled from the small-scale prototype toward a full-scale EGS field in a subsequent project. For example, scaling up the conventional seismic component would involve either (a) a stronger source and a similar number of receivers and source points but a decrease in spatial resolution roughly in proportion to the increased spatial scale, or (b) a stronger source and an increase in the number of receivers and source points in proportion to the increased spatial scale to maintain a comparable spatial resolution.

ACKNOWLEDGMENTS

We are extremely grateful to Fan-Chi Lin (University of Utah), Amanda Thomas (University of Oregon), and Marianne Karplus (University of Texas-El Paso) for contributing their Fairfield Nodal Zland 3-component sensors to our project. We thank all those who lent helping hands in the field (sorted in reverse alphabetical order by given name): Xuyang Liu, Xiangfang Zeng, Thomas Coleman, Tanner Whetstone, Stoyan Nikolov, Sin-Mei Wu, Scott Nelson, Robert Kent, Rob Skarbek, Paul Spielman, Neal Lord, Mike Cardiff, Michelle Robertson, Marianne Karplus, Lesley Parker, Kurt Feigl, John Akerley, Joe Greer, Janice Lopeman, Herb Wang, Elizabeth Berg, Dante Fratta, Craig Stenzel, Corné Kreemer, Cliff Thurber, Chelsea Lancelle, Cecil Hoffpauir, Bret Pecoraro, Bill Foxall, Ben Duggan, Athena Chalari, Andy Valentine, Amanda Thomas, and Alex Jensen. We also thank Jeff Wagoner, Drew Siler, Nicholas Hinz, and James Faulds for assistance with their geologic models.

Raw Synthetic Aperture Radar (SAR) data from the ERS, and Envisat satellite missions operated by the European Space Agency (ESA) are copyrighted by ESA and were provided through the WInSAR consortium at the UNAVCO facility. SAR data from the ALOS satellite mission operated by the Japanese Space Agency (JAXA) were acquired from NASA's Distributed Active Archive Center at the Alaska Satellite Facility (ASF). SAR data from the TerraSAR-X and TanDEM-X satellite missions operated by the German Space Agency (DLR) were acquired through Research Project RES1236.

Elena C. Reinisch was supported by the National Science Foundation Graduate Research Fellowship under grant DGE-1256259. The work presented herein was funded in part by the Office of Energy Efficiency and Renewable Energy (EERE), U.S. Department of Energy, under Award Numbers DE-EE0006760 and DE-EE0005510.

REFERENCES

Akerley, J. (2016), PoroTomo Subtask 6.8 - Brady Well Pumping Data During Deployment. http://dx.doi.org/0.15121/1334283

Ali, S. T., J. Akerley, E. C. Baluyut, M. Cardiff, N. C. Davatzes, K. L. Feigl, W. Foxall, D. Fratta, R. J. Mellors, P. Spielman, H. F. Wang, and E. Zemach (2016), Time-series analysis of surface deformation at Brady Hot Springs geothermal field (Nevada) using interferometric synthetic aperture radar, *Geothermics, 61*, 114-120. http://dx.doi.org/10.1016/j.geothermics.2016.01.008

Bakku, S. K. (2015), Fracture characterization from seismic measurements in a borehole, Ph.D. thesis, 227 pp, Massachusetts Institute of Technology.

Barry, K., D. Cavers, and C. Kneale (1975), Recommended standards for digital tape formats, *Geophysics, 40*, 344-352. http://library.seg.org/doi/abs/10.1190/1.1440530

Benioff, H., and B. Gutenberg (1952), The response of strain and pendulum seismographs to surface waves, *Bulletin of the Seismological Society of America, 42*, 229-237. http://www.bssaonline.org/cgi/content/abstract/42/3/229

Blewitt, G., C. Kreemer, W. C. Hammond, and J. Goldfarb (2013), Terrestrial reference frame NA12 for crustal deformation studies in North America, *Journal of Geodynamics, 72*, 11-24. http://dx.doi.org/10.1016/j.jog.2013.08.004

Cardiff, M., W. Barrash, and P. K. Kitanidis (2013), Hydraulic conductivity imaging from 3-D transient hydraulic tomography at several pumping/observation densities, *Water Resources Research, 49*, 7311-7326. http://dx.doi.org/10.1002/wrcr.20519

Coleman, T. (2013), A novel technique for depth discrete flow characterization: fibre optic distributed temperature sensing within boreholes sealed with flexible underground liners, MASc. thesis, University of Guelph.

Coolbaugh, M. F., C. Sladek, C. Kratt, and G. Edmondo (2004), Digital mapping of structurally controlled geothermal features with GPS units and pocket computers, *Geothermal Resources Council Transactions, 28*, 321-325.

Daley, T. M., D. E. Miller, K. Dodds, P. Cook, and B. M. Freifeld (2015), Field testing of modular borehole monitoring with simultaneous distributed acoustic sensing and geophone vertical seismic profiles at Citronelle, Alabama, *Geophysical Prospecting*. http://dx.doi.org/10.1111/1365-2478.12324

FairfieldNodal (2015), Typical specifications for FairfieldNodal ZLAND 3C seismometers, http://static.fairfieldnodal.com/assets/media/pdf/ZLand-3C-typical-specs.pdf

Faulds, J., I. Moeck, P. Drakos, and E. Zemach (2004), Structural assessment and 3D geological modeling of the Brady's geothermal area, Churchill county (Nevada, USA): A preliminary report, paper presented at Thirty-Fifth Workshop on Geothermal Reservoir Engineering, Stanford University, Stanford, California.

Faulds, J. E., and L. J. Garside (2003), Preliminary Geologic Map Of The Desert Peak - Brady Geothermal Fields, Churchill County, Nevada.

Faulds, J. E., M. F. Coolbaugh, G. S. Vice, and M. L. Edwards (2006), Characterizing Structural Controls of Geothermal Fields in the Northwestern Great Basin: A Progress Report, *Geothermal Resources Council Transactions, 30*, 69-76.

Faulds, J. E., M. F. Coolbaugh, D. Benoit, G. Oppliger, M. Perkins, I. Moeck, and P. Drakos (2010), Structural Controls of Geothermal Activity in the Northern Hot Springs Mountains, Western Nevada: The Tale of Three Geothermal Systems (Brady's, Desert Peak, and Desert Queen), *Geothermal Resources Council Transactions, 34*, 675-683.

Faulds, J. E. (2011), Assessment of favorable structural settings of geothermal systems in the great basin region, western USA, paper presented at 2011 GSA Annual Meeting in Minneapolis.

Haefner, R. J., R. A. Sheets, and R. E. Andrews (2010), Evaluation of the horizontal-to-vertical spectral ratio (HVSR) seismic method to determine sediment thickness in the vicinity of the South Well Field, Franklin County, OH, *The Ohio Journal of Science, 110*, 77.

Jolie, E., I. Moeck, and J. E. Faulds (2015), Quantitative structural–geological exploration of fault-controlled geothermal systems—A case study from the Basin-and-Range Province, Nevada (USA), *Geothermics, 54*, 54-67. http://dx.doi.org/10.1016/j.geothermics.2014.10.003

Lancelle, C. (2016), Distributed Acoustic Sensing for Imaging Near-Surface Geology and Monitoring Traffic at Garner Valley, California, Ph.D. thesis thesis, University of Wisconsin-Madison.

Lim, D., W. Barrash, and M. Cardiff (2015), Oscillatory Hydraulic Tomography at the Field Scale: Boise Hydrogeophysical Research Site (#A31B-0049), paper presented at AGU Fall Meeting, San Francisco. https://agu.confex.com/agu/fm15/meetingapp.cgi/Paper/72569

Lim, D. D. (2016), PoroTomo Subtask 6.8 - Brady Well Coordinates and Observation Sensor Depths. http://dx.doi.org/10.15121/1261986

Lin, F.-C., D. Li, R. W. Clayton, and D. Hollis (2013), High-resolution 3D shallow crustal structure in Long Beach, California: Application of ambient noise tomography on a dense seismic array, *GEOPHYSICS, 78*, Q45-Q56. http://library.seg.org/doi/abs/10.1190/geo2012-0453.1

Lord, N., H. Wang, and D. Fratta (2016a), A source-synchronous filter for uncorrelated receiver traces from a swept-frequency seismic source, *Geophysics, 81*, P47-P55. http://dx.doi.org/10.1190/geo2015-0324.1

Lord, N. E., X. Zeng, D. Fratta, K. L. Feigl, H. F. Wang, and PoroTomo_Team (2016b of Conference), Multispectral Analysis of Surface Wave (MASW) Analysis of Near-Surface Structure at Brady Hot Springs from Active Source and Ambient Noise Using a 8700-meter Distributed Acoustic Sensing (DAS) Array (abstract #S13B-2559), abstract presented at Fall Meeting Amer. Geophys. Un. https://agu.confex.com/agu/fm16/meetingapp.cgi/Paper/190705

Massonnet, D., and K. L. Feigl (1998), Radar interferometry and its application to changes in the Earth's surface, *Rev. Geophys., 36*, 441-500. http://dx.doi.org/10.1029/97RG03139

Nakamura, Y. (1989), A method for dynamic characteristics estimation of subsurface using microtremor on the ground surface, *Railway Technical Research Institute, Quarterly Reports, 30*.

Oppliger, G., M. Coolbaugh, and W. Foxall (2004), Imaging structure with fluid fluxes at the Bradys geothermal field with satellite interferometric radar (InSAR): New insights into reservoir extent and structural controls, *Geothermal Resources Council Transactions, 28*, 37-40. http://unr.edu/geothermal/pdffiles/OppligerCoolbaughFoxallGRC04.pdf

Parker, L., X. Zeng, C. H. Thurber, and PoroTomo_Team (2016 of Conference), Assessing Multiple Methods for Determining Active Source Travel Times in a Dense Array (abstract #NS23A-1923), abstract presented at Fall Meeting American Geophysical Union, San Francisco. https://agu.confex.com/agu/fm16/meetingapp.cgi/Paper/163143

Parker, T., S. Shatalin, and M. Farhadiroushan (2014), Distributed Acoustic Sensing-A New Tool for Seismic Applications, *First Break, 32*, 61 - 69 http://fb.eage.org/publication/content?id=73487

Pitz, W., and D. Miller (2010), The TerraSAR-X Satellite, *Geoscience and Remote Sensing, IEEE Transactions on, 48*, 615-622. http://dx.doi.org/10.1109/TGRS.2009.2037432

Reinisch, E. C., S. T. Ali, M. Cardiff, C. Kreemer, P. Team, and K. L. Feigl (2016a of Conference), Analysis of Interferometric Synthetic Aperture Radar Phase Data at Brady Hot Springs, Nevada, USA Using Prior Information (abstract #NS41A-1899), abstract presented at Fall Meeting American Geophysical Union, San Francisco. https://agu.confex.com/agu/fm16/meetingapp.cgi/Paper/134641

Reinisch, E. C., M. Cardiff, and K. L. Feigl (2016b), Graph theory for analyzing pair-wise data: application to geophysical model parameters estimated from interferometric synthetic aperture radar data at Okmok volcano, Alaska, *J Geod*, 1-16. http://dx.doi.org/10.1007/s00190-016-0934-5

Salvi, S., S. Stramondo, G. J. Funning, A. Ferretti, F. Sarti, and A. Mouratidis (2012), The Sentinel-1 mission for the improvement of the scientific understanding and the operational monitoring of the seismic cycle, *Remote Sensing of Environment, 120*, 164-174. http://dx.doi.org/10.1016/j.rse.2011.09.029

Shevenell, L., G. Oppliger, M. Coolbaugh, and J. Faulds (2012), Bradys (Nevada) InSAR Anomaly Evaluated With Historical Well Temperature and Pressure Data, *Geothermal Resources Council Transactions, 36*, 1383-1390.

Torres, R., P. Snoeij, D. Geudtner, D. Bibby, M. Davidson, E. Attema, P. Potin, B. Rommen, N. Floury, M. Brown, I. N. Traver, P. Deghaye, B. Duesmann, B. Rosich, N. Miranda, C. Bruno, M. L'Abbate, R. Croci, A. Pietropaolo, M. Huchler, and F. Rostan (2012), GMES Sentinel-1 mission, *Remote Sensing of Environment, 120*, 9-24. http://dx.doi.org/10.1016/j.rse.2011.05.028

Zeng, X., C. Thurber, Y. Luo, E. Matzel, and PoroTomo_Team (2016 of Conference), High-resolution shallow structure revealed with ambient noise tomography on a dense array (abstract #S13B-2574), abstract presented at Fall Meeting Amer. Geophys. Un., AGU, San Francisco. https://agu.confex.com/agu/fm16/meetingapp.cgi/Paper/151231

Zeng, X., C. Lancelle, C. Thurber, D. Fratta, H. Wang, A. Chalari, and A. Clarke (2017a), Properties of Noise Cross Correlation Functions Obtained from a Distributed Acoustic Sensing (DAS) Array at Garner Valley, California, *Bull. Seismol. Soc. Am., in press.*

Zeng, X., C. Thurber, H. Wang, D. Fratta, E. Matzel, and PoroTomo_Team (2017b), High-resolution Shallow Structure Revealed with Ambient Noise Tomography on a Dense Array, paper presented at Stanford Geothermal Workshop, Stanford University. http://geoscience.wisc.edu/geoscience/people/faculty/feigl/porotomo/